Atmos. Meas. Tech., 8, 1685–1699, 2015
www.atmos-meas-tech.net/8/1685/2015/
doi:10.5194/amt-8-1685-2015

Atmospheric Measurement Techniques
Open Access

Improved spectral fitting of nitrogen dioxide from OMI in the 405–465 nm window

J. H. G. M. van Geffen[1], K. F. Boersma[1,2], M. Van Roozendael[3], F. Hendrick[3], E. Mahieu[4], I. De Smedt[3], M. Sneep[1], and J. P. Veefkind[1,5]

[1]Royal Netherlands Meteorological Institute (KNMI), De Bilt, the Netherlands
[2]Wageningen University (WUR), Wageningen, the Netherlands
[3]Belgium Institute for Space Aeronomy (BIRA-IASB), Brussels, Belgium
[4]University of Liège (ULg), Liège, Belgium
[5]Delft University of Technology (TUDelft), Delft, the Netherlands

Correspondence to: J. H. G. M. van Geffen (geffen@knmi.nl)

Received: 16 June 2014 – Published in Atmos. Meas. Tech. Discuss.: 21 October 2014
Revised: 19 February 2015 – Accepted: 23 March 2015 – Published: 8 April 2015

Abstract. An improved nitrogen dioxide (NO_2) slant column density retrieval for the Ozone Monitoring Instrument (OMI) in the 405–465 nm spectral region is presented. Since the launch of OMI on board NASA's EOS-Aura satellite in 2004, differential optical absorption spectroscopy (DOAS) retrievals of NO_2 slant column densities have been the starting point for the KNMI DOMINO and NASA SP NO_2 vertical column data as well as the OMI NO_2 data of some other institutes. However, recent intercomparisons between NO_2 retrievals from OMI and other UV/Vis and limb spectrometers, as well as ground-based measurements, suggest that OMI stratospheric NO_2 is biased high.

This study revises and, for the first time, fully documents the OMI NO_2 retrieval in detail. The representation of the OMI slit function to convolve high-resolution reference spectra onto the relevant spectral grid is improved. The window used for the wavelength calibration is optimised, leading to much-reduced fitting errors. Ozone and water vapour spectra used in the fit are updated, reflecting the recently improved knowledge of their absorption cross section in the literature. The improved spectral fit also accounts for absorption by the O_2–O_2 collision complex and by liquid water over clear-water areas.

The main changes in the improved spectral fitting result from the updates related to the wavelength calibration: the RMS error of the fit is reduced by 23 % and the NO_2 slant column by 0.85×10^{15} molec cm^{-2}, independent of latitude, solar zenith angle and NO_2 value. Including O_2–O_2 and liquid water absorption and updating the O_3 and water vapour cross-section spectra further reduces NO_2 slant columns on average by 0.35×10^{15} molec cm^{-2}, accompanied by a further 9 % reduction in the RMS error of the fit.

The improved OMI NO_2 slant columns are consistent with independent NO_2 retrievals from other instruments to within a range that can be explained by photochemically driven diurnal increases in stratospheric NO_2 and by small differences in fitting window and approach. The revisions indicate that current OMI NO_2 slant columns suffered mostly from an additive positive offset, which is removed by the improved wavelength calibration and representation of the OMI slit function. It is therefore anticipated that the improved NO_2 slant columns are most important to retrievals of spatially homogeneous stratospheric NO_2 rather than to heterogeneous tropospheric NO_2.

1 Introduction

Nitrogen dioxide (NO_2) and nitrogen oxide (NO) – together usually referred to as nitrogen oxides ($NO_x = NO + NO_2$) – are important trace gases in the Earth's atmosphere. They enter the atmosphere due to anthropogenic (e.g. fossil fuel combustion, biomass burning) and natural (e.g. microbiological processes in soils, wild fires, lightning) processes. Over remote regions NO_2 is primarily located in the stratosphere. Stratospheric NO_2 columns range from about 2×10^{15} to

7×10^{15} molec cm^{-2} between the tropics and high latitudes. For polluted regions, up to 90 % of the total NO_2 column may be located in the troposphere. Tropospheric NO_2 columns over polluted areas are usually considerably higher, in places even higher than 30×10^{15} molec cm^{-2}. For typical levels of OH, the lifetime of NO_x in the lower troposphere is less than 1 day (e.g. Schaub et al., 2007; Beirle et al., 2011).

Boundary layer NO_2 directly affects human health (WHO, 2003). In addition, nitrogen oxides are essential precursors for the photochemical formation of ozone (Sillman et al., 1990): they influence concentrations of OH and thereby influence the lifetime of methane (Fuglestvedt et al., 1999) and other gases. NO_2 itself is a minor greenhouse gas, but the indirect effects of NO_2 on global climate change are probably larger, with a presumed net cooling effect mostly driven by oxidation-fuelled aerosol formation (Shindell et al., 2009). Stratospheric NO_2 originates mainly from oxidation of N_2O in the middle stratosphere, which leads to NO_x, which in turn acts as a catalyst for ozone destruction (Crutzen, 1970; Hendrick et al., 2012). Stratospheric NO_x can also suppress ozone depletion by converting reactive chlorine and hydrogen compounds into unreactive reservoir species (such as $ClONO_2$ and HNO_3; Murphy et al., 1993).

The important role of NO_2 in both troposphere and stratosphere requires monitoring of its concentration distribution on a global scale. Observations from satellite instruments provide global coverage complementary to sparse measurements by ground-based and in situ (balloon, aircraft) instruments. NO_2 column densities have been retrieved using the differential optical absorption spectroscopy (DOAS) technique from space since the mid-1990s from data acquired by the nadir-viewing UV/Vis backscatter instruments GOME (Burrows et al., 1999), SCIAMACHY (Bovensmann et al., 1999), OMI (Levelt et al., 2006) and the GOME-2 instruments (Munro et al., 2006) aboard MetOp-A and MetOp-B. TROPOMI (Veefkind et al., 2012), scheduled for launch in 2016, will extend the record of these observations.

The retrieval of NO_2 from satellite measured spectra with DOAS is certainly possible but not easy: the structure of the NO_2 differential absorption is weak and there are interfering signals from the surface, atmosphere and instrumental issues. Most retrievals of NO_2 concentrations are performed in the visible range between 400 and 500 nm, taking into account other absorbers and processes relevant in this wavelength range. Early satellite retrievals of NO_2 focused on the dominant absorbers NO_2, ozone and water vapour, as well as rotational Raman scattering (the so-called "Ring effect"). Recent years have shown continuous improvements in the NO_2 retrieval by accounting for weaker absorbers, notably the O_2–O_2 collision complex and liquid water.

This paper describes a revision of NO_2 slant column retrieval from level-1b spectra measured by OMI since 2004, performed by a processor named OMNO2A. The study was prompted by the observation, reported first by N. Krotkov at the EOS-Aura meeting in October 2012 (Krotkov et al., 2012), that OMI stratospheric NO_2 concentrations are systematically higher than those derived from SCIAMACHY and GOME-2 measurements by 0.5–1 $\times 10^{15}$ molec cm^{-2}, after accounting for the daytime increase in stratospheric NO_2 (Dirksen et al., 2011). Recently, Belmonte-Rivas et al. (2014) confirmed the high bias in OMI stratospheric columns compared to an ensemble of stratospheric NO_2 retrievals from satellite-based limb-sounding sensors. Section 3 presents a further comparison of OMI, SCIAMACHY and GOME-2 data, as well as a comparison using ground-based measurements at the Jungfraujoch station, to confirm the high bias in OMI NO_2 data.

The revision of the OMNO2A settings and input is further motivated by a number of issues regarding the absorption reference spectra (Sect. 4.1): (a) the need to update the spectra of ozone and water vapour; (b) the need to account for the wavelength and row dependency of the OMI slit function in the convolution of the spectra; (c) the need to investigate whether including absorption by O_2–O_2 (so far omitted from OMNO2A; cf. Bucsela et al., 2006) and liquid water (cf. Richter et al., 2011; Lerot et al., 2010) improves the NO_2 retrieval results. In addition, the effects on the DOAS NO_2 retrieval of the wavelength calibration of the OMI radiance spectra, introduced in OMNO2A following the first appearance of the so-called row anomaly in 2007 but not yet evaluated, has been investigated and the calibration settings have been optimised (Sect. 4.2). Lastly, it was recognised that it is important for users of the OMI NO_2 data to document the essential elements, both the current and the updated, of the slant column retrieval in one easily referable paper.

2 Observations of NO_2 column densities

2.1 UV/Vis satellite-based NO_2 observations

The main focus of this paper is NO_2 data derived from measurements by OMI (Levelt et al., 2006), which are compared to NO_2 data from the first GOME-2 instrument (Munro et al., 2006) and from SCIAMACHY (Bovensmann et al., 1999). All three instruments measure the backscattered and direct sunlight in the UV and visible ranges from a sun-synchronous polar orbit.

OMI is aboard the EOS-Aura satellite and has been operating since 2004. The overpass is at 13:40 local time (LT), with the satellite flying south to north on the dayside of the Earth. Individual nadir ground pixels are 13×24 km^2 at the middle of the swath; the size of the pixels increases towards the edges of the swath. The full swath width is about 2600 km and OMI achieves global coverage each day.

The first GOME-2 instrument is aboard the MetOp-A satellite and has been operating since 2007. The overpass is at 09:30 LT, with the satellite flying north to south on the dayside of the Earth. Individual ground pixels are 40×80 km^2. The full swath width is about 1920 km and GOME-2 achieves nearly global coverage each day. A sec-

Table 1. Main settings of the DOAS retrieval of NO_2 slant column densities of the data versions used in this paper for the satellite instruments OMI, GOME-2 and SCIAMACHY; for OMI the current settings and the settings resulting from the discussion in this paper are given.

	OMI – current	OMI – updated	GOME-2	SCIAMACHY
Wavelength range (nm)	405–465	405–465	425–450	426.5–451.5
Secondary trace gases	O_3, H_2O_{vap}	O_3, H_2O_{vap}, O_2–O_2, H_2O_{liq}	O_3, H_2O_{vap}, O_2–O_2	O_3, H_2O_{vap}, O_2–O_2
Pseudo-absorbers	Ring	Ring	Ring	Ring
Degree of polynomial	5	5	3	2
Fitting method	non-linear	non-linear	linear	linear
Offset fitted	no	no	yes	yes
DOAS retrieval code	OMNO2A	OMNO2A	QDOAS	QDOAS
Retrieval responsible	KNMI	KNMI	BIRA-IASB	BIRA-IASB
Data version used	DOMINO v2.0	DOMINO v3.0	TM4NO2A v2.1	TM4NO2A v2.0

ond, identical GOME-2 instrument was launched aboard the MetOp-B satellite in 2012. In this paper, GOME-2 refers to the instrument aboard MetOp-A, sometimes referred to as GOME-2A.

SCIAMACHY is aboard the satellite ENVISAT and operated in the period 2002–2012. The overpass was at 10:00 LT, with the satellite flying north to south on the dayside of the Earth. Individual ground pixels were $30 \times 60\,km^2$. The full swath width was about 960 km and SCIAMACHY achieved global coverage only once every 6 days, because it measured alternatively in a nadir and limb viewing mode.

The DOAS retrieval technique, described in Sect. 2.2, is applied to the backscattered spectra measured by the three satellite instruments to obtain the NO_2 slant column density (SCD). The SCD is the integrated concentration of NO_2 over light paths from the Sun through the Earth's atmosphere to the satellite, weighted with their relative contribution to the radiance.

The standard OMI NO_2 SCD data are calculated at NASA by a processor named OMNO2A. The retrieval results of OMNO2A are input for subsequent processing to determine NO_2 vertical column densities (VCDs), e.g. for the DOMINO data product of KNMI (e.g. Boersma et al., 2007, 2011; Dirksen et al., 2011) and NASA's NO_2 Standard Product (SP; e.g. Bucsela et al., 2006, 2013). For the OMI NO_2 retrieval, the selected spectral fitting window is 405–465 nm, wider than the often used 425–450 nm window in order to improve the effective signal-to-noise ratio.

For GOME-2 and SCIAMACHY NO_2 SCD data, BIRA-IASB uses a processor based on QDOAS (Danckaert et al., 2012), the multi-platform successor of their WinDOAS package; see e.g. Van Roozendael et al. (2006) and Lerot et al. (2009). The DOAS fit on GOME-2 and SCIAMACHY data uses almost the same wavelength window: 425.0–450.0 and 426.5–451.5 nm respectively (the small difference between the fit windows is related to instrumental issues). The degree of the DOAS polynomial is 3 for GOME-2 and 2 for SCIAMACHY.

Table 1 provides an overview of the details of the DOAS retrieval for the OMI, GOME-2 and SCIAMACHY sensors used in this study.

2.2 DOAS retrieval of NO_2 slant column densities

The DOAS (Platt, 1994; Platt and Stutz, 2008) technique matches an analytical function that describes the relevant atmospheric physical processes (scattering, reflection and absorption) to the satellite-measured spectrum. In the OMNO2A setup, the modelled reflectance is expressed in terms of intensities, which leads to a non-linear fit problem and allows the effects of inelastic scattering to be described after a scattering event has occurred:

$$R_{\mathrm{mod}}(\lambda) = P(\lambda) \cdot \exp\left[-\sum_{k=1}^{N_k} \sigma_k(\lambda) \cdot N_{\mathrm{scd},k}\right] \cdot \left(1 + C_{\mathrm{Ring}} \frac{I_{\mathrm{Ring}}(\lambda)}{I_0(\lambda)}\right) . \quad (1)$$

This physical model contains a low-order polynomial $P(\lambda)$ of degree N_p that represents the slowly varying broad-band absorption, as well as Rayleigh and Mie scattering processes in the atmosphere and smooth surface reflection and absorption effects. Furthermore, the physical model includes the spectrally varying absorption signatures $\sigma_k(\lambda)$ and the slant column amount $N_{\mathrm{scd},k}$ of relevant absorbers k, notably NO_2, ozone (O_3) and water vapour (H_2O_{vap}).

The physical model accounts for inelastic Raman scattering of incoming sunlight by N_2 and O_2 molecules that leads to filling-in of the Fraunhofer lines in the radiance spectrum – the so-called "Ring effect" (see Grainger and Ring, 1962; Chance and Spurr, 1997) – by describing these effects as a pseudo-absorber, that is, by including a Ring reference absorption spectrum along with the molecular absorption terms. In Eq. (1), C_{Ring} is the Ring fitting coefficient and $I_{\mathrm{Ring}}(\lambda)/I_0(\lambda)$ the sun-normalised synthetic Ring spectrum. The term between parentheses in Eq. (1) describes both the contribution of the direct differential absorption (i.e. the 1) and the modification of these differential structures by in-

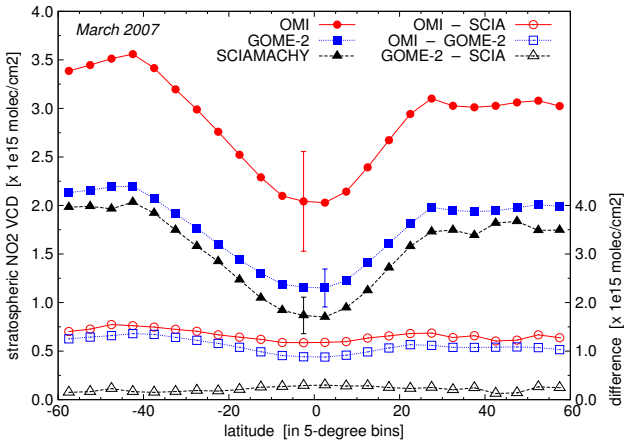

Figure 1. Monthly average stratospheric NO_2 VCD values (left axis; filled symbols) and absolute differences (right axis; open symbols) in 10^{15} molec cm^{-2} of OMI, GOME-2 and SCIAMACHY in March 2007 over the Pacific Ocean area (60° S–60° N, 140–180° W), as a function of latitude. The error bars at the data points near the equator mark for that latitude bin the average standard deviation of the total VCD (data source: http://www.temis.nl/).

elastic scattering (the $+C_{\mathrm{Ring}}\, I_{\mathrm{Ring}}(\lambda)/I_0(\lambda)$ term) to the reflectance spectrum.

The DOAS procedure minimises the difference between the measured reflectance spectrum $R_{\mathrm{meas}}(\lambda)$ and the modelled spectrum $R_{\mathrm{mod}}(\lambda)$ within a given wavelength window, in the form of minimisation of a chi-squared merit function. The measured reflectance $R_{\mathrm{meas}}(\lambda)$ is determined from the radiance measured at top-of-atmosphere $I(\lambda)$ and the measured extraterrestrial solar irradiance spectrum $I_0(\lambda)$. Some further details on the OMI NO_2 DOAS slant column retrieval, such as the merit function that is minimised and the definition of the RMS error, can be found in Sect. S1 in the Supplement.

3 Intercomparisons of stratospheric NO_2 columns

NO_2 data from OMI, GOME-2 and SCIAMACHY are evaluated for 2007. Stratospheric NO_2 concentrations are best detected over the Pacific Ocean, where tropospheric contributions to the NO_2 column are small in the absence of substantial sources of pollution. The Pacific Ocean area is defined here as the area from 60° S to 60° N and from 140 to 180° W. DOMINO v2.0 data are used for OMI (Boersma et al., 2011), TM4NO2A v2.1 for GOME-2 and TM4NO2A v2.0 for SCIAMACHY (Boersma et al., 2004).

Figure 1 shows the monthly average stratospheric NO_2 column for the three instruments and their mutual differences as a function of latitude for March 2007; for other months (not shown) the comparisons look quite similar. The OMI stratospheric columns are clearly higher than those of GOME-2 by about 1.0×10^{15} molec cm^{-2}, consistent with Belmonte-Rivas et al. (2014), who reported a similar high bias in OMI and low bias in SCIAMACHY data relative to stratospheric NO_2 columns obtained from an ensemble of limb and nadir sensors. The GOME-2 stratospheric columns (not included in the study of Belmonte-Rivas et al., 2014) in turn are higher than those of SCIAMACHY by 0.1–0.3×10^{15} molec cm^{-2}.

Table 2. Average differences in stratospheric NO_2 columns over the Pacific Ocean area (60° S–60° N, 140–180° W) of 2007 of OMI, GOME-2 and SCIAMACHY, where the averages are computed from monthly latitudinally binned data. The relative difference (right column) is given as percentage of the column values of the second instrument in the difference, e.g. w.r.t. SCIA in the difference OMI − SCIA (data source: http://www.temis.nl/).

Instruments	Absolute values [$\times 10^{15}$ molec cm^{-2}]	Relative difference [%]
OMI – SCIA	$+1.28 \pm 0.15$	$+80.1 \pm 9.6$
OMI – GOME-2	$+1.14 \pm 0.18$	$+65.6 \pm 10.3$
GOME-2 – SCIA	$+0.14 \pm 0.09$	$+8.7 \pm 5.8$

Figure 1 shows that there is only a weak variability of the intra-sensor differences with latitude and that the differences are similar to within 0.2×10^{15} molec cm^{-2}. This weak variability with latitude and independence of the month indicates that the differences between the instruments is dominated by an additive offset. Table 2 lists the annual averaged 2007 intra-sensor differences over the Pacific Ocean area. The difference of 1.1–1.3×10^{15} molec cm^{-2} between OMI (overpass at 13:40 LT) and the two mid-morning sensors is considerably larger than the increase of stratospheric NO_2 between the respective measurement times. Photochemical models suggest a latitude-dependent increase of 10–30 % in stratospheric NO_2 between 09:30 and 13:40 LT. This increase reflects the production of NO_2 from N_2O_5 photodissociation and corresponds to an increase of 0.1–0.6×10^{15} molec cm^{-2} (Dirksen et al., 2011; Belmonte-Rivas et al., 2014).

The comparison of data from the ground-based SAOZ and FTIR instruments at the Jungfraujoch station with satellite data by Hendrick et al. (2012) was repeated, now also including OMI data and extending the GOME-2 and SCIAMACHY data sets to the end of 2012 (see Sect. S2 in the Supplement). The results of the comparisons also strongly suggest that OMI stratospheric NO_2 is biased high. Since the air-mass factor calculations for NO_2 in the stratosphere are straightforward (with an error of less than 1 %), the high bias in OMI stratospheric columns originates from the slant column retrieval. As a result of this finding, the details of the OMI NO_2 spectral fitting OMNO2A were revisited.

4 Improvements to the OMI NO_2 retrieval

4.1 Reference spectra

The set of reference spectra in the current OMNO2A processing has been introduced in August 2006. Since then a number of improved reference spectra data sets have been reported in the peer-reviewed literature. In addition, the reference spectra used in the current OMNO2A processing have been convolved with the OMI slit function, described by a parametrised broadened Gaussian function (Dirksen et al., 2006), but without taking the wavelength and row dependency (i.e. viewing angle dependency) of the slit function into account.

For these reasons all relevant cross sections are generated anew, based on the latest established absorption spectra, and convolved with the OMI slit function while now taking the wavelength and row dependency of the slit function into account in the form of a row-average slit function. The OMI slit function [1] and the implementation of the convolution are given in Sect. S3 in the Supplement.

Details of the relevant reference spectra used in the current and forthcoming OMNO2A slant column fit are given in Sect. S4. The updated reference spectra are

- solar spectrum $I_{\mathrm{ref}}(\lambda)$, from Dobber et al. (2008)
- NO_2 absorption, from Vandaele et al. (1998)
- O_3 absorption, from Bogumil et al. (2000), version 3.0 (Dec. 2004)
- water vapour (H_2O_{vap}) absorption, based on the HITRAN 2012 database (Rothman et al., 2013)
- O_2–O_2 absorption, from Thalman and Volkamer (2013)
- liquid water (H_2O_{liq}) absorption, from Pope and Fry (1997)
- Ring radiance spectrum $I_{\mathrm{Ring}}(\lambda)$, computed following Chance and Spurr (1997).

The reference spectra labelled "v2006" below refer to those used in the current OMNO2A processor (used in, for example, the DOMINO v2.0 data set), while "v2014" refers to the updated reference spectra. The relation between these labels and the official version numbering of OMNO2A is described in Sect. S5.

[1] The full set of the OMI slit function – the slit functions for the 60 individual rows as well as the average slit function, both for the visible (350–500 nm) and UV (310–380 nm) wavelength ranges – is available for download via the OMI website at http://www.knmi.nl/omi/research/product/ .

4.1.1 Other absorption features

Over tropical forests, detectable contributions from glyoxal (CHOCHO) have been reported, and its retrieval requires the inclusion of NO_2 absorption (e.g. Lerot et al., 2010). Conversely, however, glyoxal absorption is only a very minor interference for NO_2 absorption, so that it can be safely neglected.

Richter et al. (2011) have investigated absorption signatures attributable to sand, e.g. over deserts, but this signature is broadband in the OMI NO_2 fit window (any structure in the signature lies well beyond the fit window) and is therefore not accounted for here.

Absorption by vibrational Raman scattering (VRS; e.g. Vasilkov et al., 2002; Vountas et al., 2003) is known to play a role over open waters and thus may have an impact on the NO_2 retrieval; however, it is unclear whether including VRS improves the retrieval results, partly because its signature is apparent over areas where it certainly is not playing a role, e.g. over deserts (A. Richter, personal communication, 2014). In addition, the VRS signature does not seem to be independent from the signature of liquid water absorption (Peters et al., 2014). For these reasons, absorption by VRS is not investigated here.

4.2 Wavelength calibration

The measured solar irradiance spectrum $I_0(\lambda)$ used in the OMI NO_2 DOAS fit has been constructed from a yearly average of daily solar irradiance measurements by OMI during 2005 and has an accurate wavelength calibration.

From the start of the OMI mission, the level-1b radiance spectra $I(\lambda)$ of OMI are given on an initial assigned wavelength grid (Voors et al., 2006). This assigned wavelength grid – hereafter referred to as "wcA" – was at the time accurate enough for the NO_2 retrieval with OMNO2A. After the onset of the first row anomaly [2] in June 2007 and the subsequent growth of this issue after May 2008, however, the assigned wavelength grid appeared to be less accurate and, consequently, hampered sufficiently accurate NO_2 retrievals in all rows, including those not affected by the row anomaly.

The NO_2 fit results were improved by the introduction of a wavelength calibration in OMNO2A in January 2009. This wavelength calibration determines a wavelength shift for each individual radiance spectrum $I(\lambda)$ from a fit against the reference solar spectrum $I_{\mathrm{ref}}(\lambda)$, taking the Ring effect into account (cf. Voors et al., 2006), starting from the assigned wavelength grid wcA. The wavelength calibration in the current OMNO2A processing, called "wcB" hereafter, uses 408.0–423.0 nm as the calibration window. This window was chosen because it covers some distinct Fraunhofer features in the solar spectrum. Due to the construction of the OMI detector, a squeezing or stretching of the wave-

[2] See http://www.knmi.nl/omi/research/product/rowanomaly-background.php for an explanation and details.

Table 3. Pacific Ocean test orbit average main results of the wavelength calibration and spectral fit, using the v2014 reference spectra for the wavelength calibration windows mentioned in Sect. 4.2.

	Calib. window		Shift	RMS	NO_2 error
	Begin	End	$\times 10^{-3}$	$\times 10^{-4}$	$\times 10^{15}$
Name	(nm)	(nm)	(nm)	(–)	(molec cm^{-2})
wcB	408.0	423.0	−3.63	0.97	0.99
wcN	409.0	428.0	−4.68	0.95	0.97
wcC	425.5	443.0	−7.70	1.09	1.10
wcF	405.0	465.0	−6.83	1.02	1.04

lengths is unlikely (which is confirmed by ongoing tests on OMI data as preparation for the implementation of a wavelength calibration for TROPOMI which includes the possibility of a squeeze/stretch in the calibration), so that the shift found from the calibration window is representative for the whole NO_2 fit window. The relation between the wavelength calibration labels and the official version numbering of OMNO2A is described in Sect. S5.

With the update of the solar reference spectrum $I_{\mathrm{ref}}(\lambda)$ and the Ring radiance spectrum $I_{\mathrm{Ring}}(\lambda)$, the wavelength shift determined in calibration window wcB turns out to be different from the shift found in the current OMNO2A setup. This change in the wavelength grid of the level-1b spectra directly improves the fit results: both the RMS and the error on the NO_2 SCD are reduced. Using the v2006 reference spectra for NO_2, O_3 and H_2O_{vap} (and not yet including O_2–O_2 and H_2O_{liq}), the changes due to the introduction of the new solar and Ring reference spectra in the wcB wavelength calibration, averaged between 60° S and 60° N over the Pacific Ocean test orbit (see Sect. 5.1), are as follows:

- wavelength shift from $+0.55$ to -3.63×10^{-3} nm
- RMS error from 1.39 to 1.15×10^{-4} (−17.4 %)
- NO_2 error from 1.29 to 1.17×10^{15} molec cm^{-2} (−9.2 %)
- NO_2 SCD from 8.54 to 8.04×10^{15} molec cm^{-2} (−5.8 %).

Since the spectral sampling of OMI is about 0.21 nm (Levelt et al., 2006), a shift of -3.62×10^{-3} nm corresponds to 1.7 % of a wavelength pixel.

Given that the NO_2 fit results depend so clearly on the wavelength calibration, it was decided to test a range of calibration windows. Both the starting and end point of the calibration window were varied in steps of 0.5 nm, with a minimum size of 10 nm for the window, over the complete 405–465 nm fit window for a total of 5151 possible calibration windows. The fits were performed on the Pacific Ocean test orbit with all new v2014 reference spectra, including O_2–O_2 and H_2O_{liq} absorption. From these calculations the "optimal calibration window", defined as the window that results in the lowest RMS and NO_2 error in the subsequent DOAS fit, was found to be 409.0–428.0 nm. This new calibration window, hereafter "wcN", covers one more distinct Fraunhofer line than wcB (cf. Fig. S4 in the Supplement).

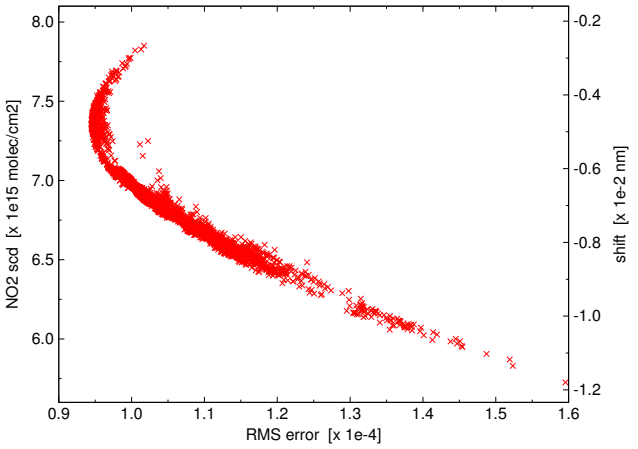

Figure 2. Pacific Ocean test orbit average relationship between the RMS error and the NO_2 SCD for the 5151 wavelength calibration windows investigated. The right axis of the main plot is an approximation: it gives the wavelength shift constructed from the linear relationship with the NO_2 SCD mentioned in the text.

Table 3 lists the calibration shift and the RMS and NO_2 error of the subsequent DOAS fit for calibration windows wcB and wcN. For comparison, Table 3 also gives the fit results using two other calibration windows: one spanning the full fit window ("wcF") and one more or less at the centre of the fit window ("wcC"). For the other orbits of the same day (not shown), minimal RMS is achieved either in the wcN window or in a slightly different window, but the difference between that RMS and the RMS of wcN is less than 0.05 %. Hence, wcN is selected as the optimal wavelength calibration window to be implemented in the new version of the OMNO2A processor.

4.2.1 Uncertainty in NO_2 SCD related to calibration

Figure 2 shows the relationship between the RMS error (horizontal axis) and the resulting NO_2 SCD (left exist) for all calibration windows of the Pacific Ocean test orbit. The minimum RMS is achieved for calibration window wcN (409.0–428.0). There are 112 possible calibration windows with an RMS within 0.5 % of the RMS of wcN, and these calibration windows all have an end-wavelength below 430 nm. For these windows, the NO_2 error ranges from 0.97 (the value for wcN) to 0.98×10^{15} molec cm^{-2}, and the NO_2 SCD ranges from 7.23 to 7.47×10^{15} molec cm^{-2}. The latter variation can be considered a measure for the uncertainty in the NO_2 SCD related to the wavelength calibration: 0.12×10^{15} molec cm^{-2} (0.05×10^{15} molec cm^{-2} in terms of the NO_2 VCD when using a geometric air-mass factor).

Table 4. Results of the NO_2 SCD fit for the different steps of the updates of the OMNO2A processing for the Pacific Ocean orbit. Case 0 represents the current OMNO2A version (v1) and case 4 is the updated version (v2) settings. Cases 1 through 4 follow the updates listed at the beginning of Sect. 5. The numbers between parentheses are percentage changes w.r.t. case 0. The NO_2 SCD error is given in absolute value and as percentage of the NO_2 SCD column. The NO_2 VCD in the last column is determined from the SCD and the geometric air-mass factor.

Case	Solar Ring	Calib. window	NO_2, O_3 H_2O_{vap}	O_2–O_2 H_2O_{liq}	RMS error (–)	NO_2 SCD (molec cm^{-2})	NO_2 SCD error (molec cm^{-2})	(%)	NO_2 VCD (molec cm^{-2})
0	v2006	wcB	v2006	no	1.39×10^{-4}	8.54×10^{15}	1.29×10^{15}	15.1	3.10×10^{15}
1	v2014	wcB	v2006	no	1.15 (−17.4 %)	8.04 (−5.8 %)	1.17 (−9.2 %)	14.5	2.92 (−6.1 %)
2	v2014	wcN	v2006	no	1.13 (−18.7 %)	7.75 (−9.2 %)	1.16 (−10.1 %)	14.9	2.81 (−9.6 %)
3	v2014	wcN	v2014	no	1.06 (−23.6 %)	7.96 (−6.8 %)	1.09 (−15.2 %)	13.7	2.89 (−7.0 %)
4	v2014	wcN	v2014	yes	0.94 (−32.0 %)	7.38 (−13.5 %)	0.97 (−24.6 %)	13.1	2.68 (−13.7 %)

There appears to be an almost perfectly linear relationship between the NO_2 SCD and the shift of the calibration for the investigated range of wavelength shifts: NO_2 SCD $[\times 10^{15}$ molec cm$^2] = 2.325 \cdot$ shift $[\times 10^{-2}$ nm$] + 8.470$, with a correlation coefficient of $r = 0.99997$. This linear relationship implies that an error in the wavelength shift of 1×10^{-3} nm (0.5 % of a detector pixel) corresponds to a change in the NO_2 SCD of about 0.2×10^{15} molec cm^{-2}. Depending on the desired accuracy of the retrieved NO_2 column, e.g. for future satellite missions, the relationship poses firm requirements on the accuracy of the wavelength grid. The effect of spectral misalignments, i.e. a mismatch between the wavelengths of the measured spectra and the reference spectra, on DOAS fit results has also been investigated, e.g. by Stutz and Platt (1996) and Beirle et al. (2013).

5 Results of the OMI NO_2 retrieval improvements

The improvements for the OMNO2A NO_2 SCD retrieval discussed above comprise four steps:

1. the update of the high-resolution solar reference spectrum and the Ring spectrum used for the wavelength calibration;
2. the change of the wavelength calibration window from wcB to wcN;
3. the update of the reference spectra of NO_2, O_3 and H_2O_{vap};
4. the inclusion of absorption by the O_2–O_2 collision complex and by liquid water.

The current OMNO2A processing system is referred to as "v1" below, while the processing using the updated spectral fit settings is named "v2".

5.1 Current vs. updated NO_2 fit results

For the comparison of the current and updated OMNO2A spectra fit results, the OMI orbit over the Pacific Ocean on 1 July 2005 (orbit number 05121) is used. Other orbits of this day and of some other days in 2005 are used to evaluate the robustness of the findings. Only ground pixels with a solar zenith angle less than 75° are considered; in most comparisons using orbit averages, the data are limited to the latitude range $[-60° : +60°]$. Since stratospheric NO_2 is the main focus of this study, no filtering of cloudy pixels is applied.

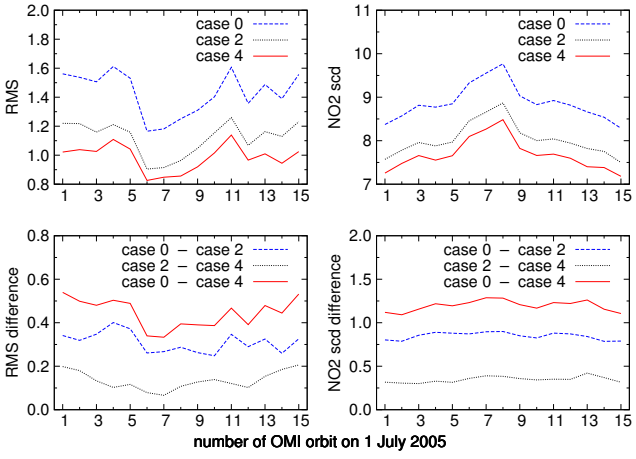

Figure 3. Absolute values (top row) and absolute differences (bottom row) of the orbit average RMS error (left column, $\times 10^{-4}$) and NO_2 SCD (right column, $\times 10^{15}$ molec cm^{-2}) as a function of the OMI orbit number on 1 July 2005; the Pacific Ocean orbit is number 14. The case numbers refer to the cases listed in Table 4. The difference "case 0 – case 2" (blue line) refers to the updates of the wavelength calibration, "case 2 – case 4" (black line) to the updates of the reference spectra, and "case 0 – case 4" (red line) to all updates put together.

Table 4 lists the NO_2 SCD, the NO_2 SCD error and the RMS error values for the step-by-step improvements listed above. The first case in the table represents the current OMNO2A settings for the SCDs used in the DOMINO v2.0 and NASA SP v2.1 NO_2 data products; case 2 represents the improved wavelength calibration; and case 4 the implementation of all updates together, i.e. the updated "v2" version of

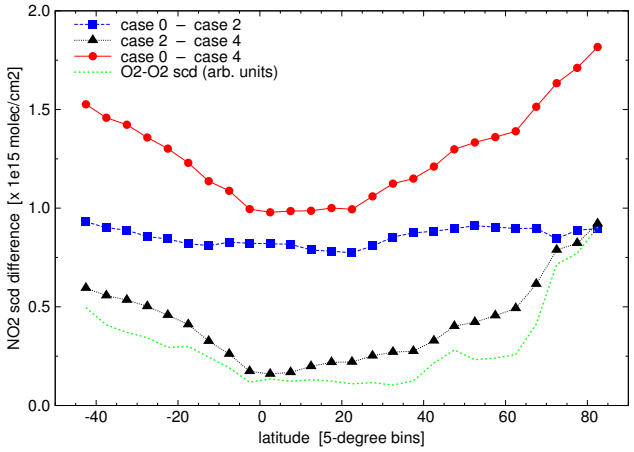

Figure 4. Absolute differences in the NO_2 SCD as a function of latitude averaged over all 15 orbits. The case numbers refer to the cases listed in Table 4, similar to the bottom panels of Fig. 3. For comparison, the concentration of O_2–O_2 as a function of latitude is shown in arbitrary units (green short-dashed line).

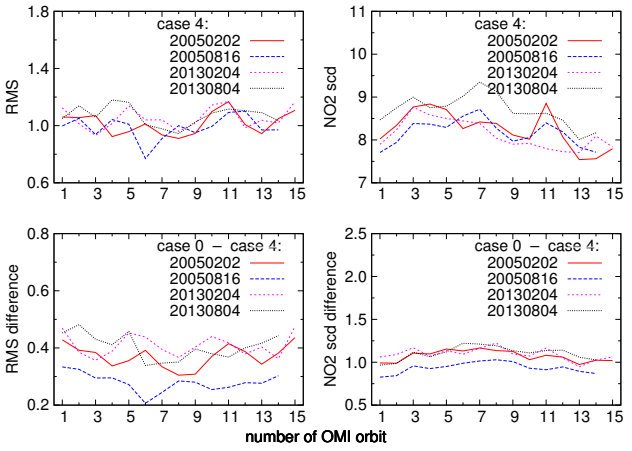

Figure 5. Absolute values of the updated data (case 4, top row) and absolute differences between the current and the updated data (bottom row) of the orbit average RMS error (left column, $\times 10^{-4}$) and NO_2 SCD (right column, $\times 10^{15}$ molec cm^{-2}) as a function of the OMI orbit number on 4 selected days. The case numbers refer to the cases listed in Table 4. Measurements from the rows affected by the row anomaly in the 2013 (rows 25–48 and 53) have been omitted from all data in this comparison.

OMNO2A. Figure 3 shows the absolute values of and differences between cases 0, 2 and 4 in Table 4 of the RMS error and the NO_2 SCD for all 15 orbits of 1 July 2005.

These results show that the wavelength calibration update (case 2) leads to large improvements in the spectral fitting of OMI NO_2 and the updates of the relevant reference spectra lead to smaller yet still significant improvements of the fit. The lower panels indicate that differences in RMS and NO_2 SCD vary only a little from orbit to orbit. When averaging the 15 orbit averages and giving changes w.r.t. the case-0 averages, the conclusions are that

- the wavelength calibration updates reduce the RMS by 23 % and the SCD by 0.85×10^{15} molec cm^{-2},
- updates in the reference spectra further reduce the RMS by 9 % and the SCD by 0.35×10^{15} molec cm^{-2},
- in total the RMS improves by 31 % and the SCD is smaller, on average, by 1.20×10^{15} molec cm^{-2}.

The latitudinal dependency of the changes in the NO_2 SCD averaged over the 15 orbits is shown in Fig. 4. The change in NO_2 SCD resulting from the update of the wavelength calibration (blue line with squares) shows little variation with latitude, indicating that the imperfect wavelength calibration likely represents an additive offset of $0.85 \pm 0.04 \times 10^{15}$ molec cm^{-2} in the current "v1 OMNO2A" retrieval.

However, the change in NO_2 SCD due to the update of the trace gas reference spectra and the inclusion of absorption by O_2–O_2 and H_2O_{liq} (black line with triangles in Fig. 4) depends clearly on latitude in absolute numbers and as a percentage of the NO_2 SCD: the change ranges from 0.1×10^{15} molec cm^{-2} (3 %) in the tropics to 0.8×10^{15} molec cm^{-2} (5 %) at high latitudes. The change in the NO_2 SCD increases with latitude and reflects the inclusion of O_2–O_2 absorption, which increases poleward as shown by the green short-dashed line in Fig. 4.

Overall, the improved OMNO2A NO_2 SCD is reduced by 1.0 to 1.8×10^{15} molec cm^{-2} (10 to 16 %), the NO_2 SCD error by 0.2 to 0.3×10^{15} molec cm^{-2} (16 to 30 %) and the RMS error by 24 to 35 %, depending on latitude.

The above settings of case 0 and case 4 have been evaluated on the 4 test days used in the EU FP7 project QA4ECV [3] to evaluate the robustness of the improvements for other days of the test year (2 February and 16 August 2005) and for more recent OMI data (4 February and 4 August 2013). Figure 5 shows the orbit average values of the RMS error and the NO_2 SCD the updated retrieval values and the differences between the current and the updated values. The other fit coefficients (not shown), such as ozone and water vapour, as well as the associated error terms, show no systematic differences between the results of the current and updated settings either. This comparison confirms that the improvements are robust over time and can therefore be used for reprocessing the entire OMI record.

To facilitate a comparison of the improved spectral fit for OMI with data from SCIAMACHY, the NO_2 slant columns of both instruments are converted to vertical columns with the geometric air-mass factor M_{geo}, taking the curvature of the Earth's atmosphere into account (Leue, 1999). This conversion ensures that the considerable differences in viewing

[3] See http://www.qa4ecv.eu/.

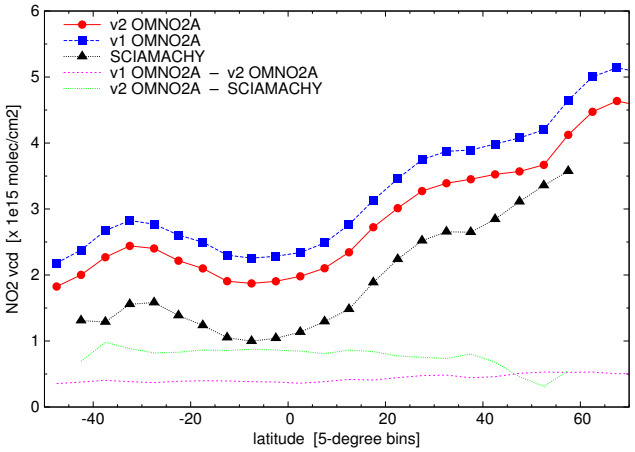

Figure 6. Comparison of the NO_2 VCD values (lines with symbols) of the new v2 OMNO2A (red circles) and old v1 OMNO2A (blue squares) retrieval for the Pacific Ocean orbit of 1 July 2005 and the average SCIAMACHY data (black triangles) over Pacific Ocean of the same day. The two lines without symbols show differences between the NO_2 VCD values. A comparison between OMI and SCIAMACHY should be limited to latitudes below 45°, because for higher latitudes the instruments cover different geographic areas.

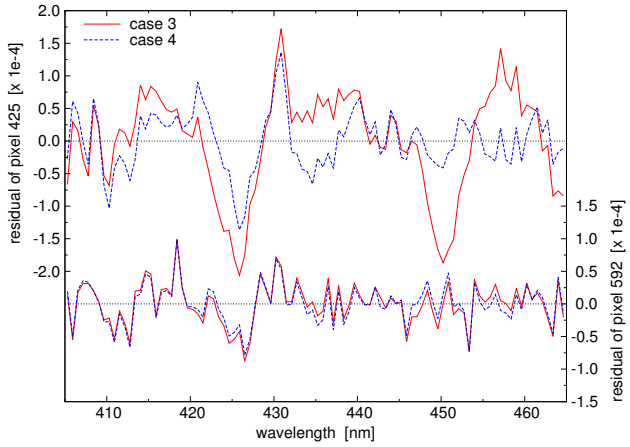

Figure 7. Spectral residual of the NO_2 retrieval fit with the updated reference spectra without (case 3, red solid lines) and with (case 4, blue dashed lines) O_2–O_2 and H_2O_{liq} absorption included for two ground pixels along row 29 (0-based): pixel 425 (located at 20.2° S, 135.4° W; top two curves, left axis) and pixel 592 (0.0° S, 139.8° W; bottom two curves, right axis) of the Pacific Ocean test orbit. To clarify the graph, the wavelengths of three detector pixels are averaged, thus mimicking the fact that OMI's spectral resolution is about 3 times its spectral sampling.

angles between the two instruments do not affect the comparison.

Figure 6 shows a comparison of the OMI Pacific Ocean test orbit using the "v1 OMNO2A" and the "v2 OMNO2A" retrieval and of the SCIAMACHY data over the Pacific Ocean of the same day (lines with symbols). Given SCIAMACHY's poor geographic coverage, the data of its three orbits over the Pacific are averaged for this comparison. The figure shows that the discrepancy between OMI and SCIAMACHY has been reduced from 1.2 to 0.8×10^{15} molec cm^{-2}.

The remaining offset between the new v2 OMNO2A and the SCIAMACHY NO_2 VCDs of 0.8×10^{15} molec cm^{-2} can be explained in part by the difference of about 0.5×10^{15} molec cm^{-2} expected due to the diurnal cycle of stratospheric NO_2. It should, furthermore, be kept in mind that SCIAMACHY has a negative bias of 0.1–0.2×10^{15} molec cm^{-2} w.r.t. GOME-2 (Sect. 3; Hendrick et al., 2012) and w.r.t. an ensemble of stratospheric NO_2 limb sensor measurements (Belmonte-Rivas et al., 2014). In addition, the OMI NO_2 is retrieved by OMNO2A with a non-linear fit approach in the 405–465 nm window, while the SCIAMACHY NO_2 is retrieved by QDOAS with a linear fit approach in the 425–450 nm window (cf. Table 1). The difference in fit window and fit approach explains another 0.1–0.2×10^{15} molec cm^{-2} in the difference between OMNO2A and SCIAMACHY, as is shown in Sect. 5.3.

5.2 About including O_2–O_2 and liquid water

The spectral residual of the NO_2 retrieval describes the unexplained portion of the measured spectrum after a selected set of absorption signatures is accounted for in the fit model. Figure 7 shows the spectral residual of two cloud-free pixels along row 29 (0-based) of the Pacific Ocean test orbit: pixel 425 and pixel 592 using the updated reference spectra without (case 3, red solid lines) and with (case 4, blue dashed lines) taking absorption of O_2–O_2 and H_2O_{liq} into account. Pixel 425 is over clear open ocean water with a low chlorophyll concentration [4] (0.028 mg m^{-3}), while pixel 592 is over ocean water with a relatively high chlorophyll concentration (0.351 mg m^{-3}). An anti-correlation between the chlorophyll concentration and the liquid water absorption coefficient is expected, because the higher the chlorophyll concentration the more opaque the water is and therefore the shorter the penetration depth of light will be.

Figure 7 shows that the residual of pixel 425 has a clear structure in the range 445–465 nm in case liquid water absorption is not accounted for, while this structure does not appear for pixel 592. If H_2O_{liq} is included in the fit, the residual of pixel 425 is much reduced (the RMS decreases by −35 %), while there is hardly any change in the residual of pixel 592 (by −2 %). For both pixels the NO_2 SCD reduces by about

[4] Chlorophyll concentrations are extracted from NASA's daily assimilated total chlorophyll data sets with the Giovanni online data system from NASA GES DISC; data file: NOBM_DAtot.CR.data.01Jul2005.G3.output.txt.

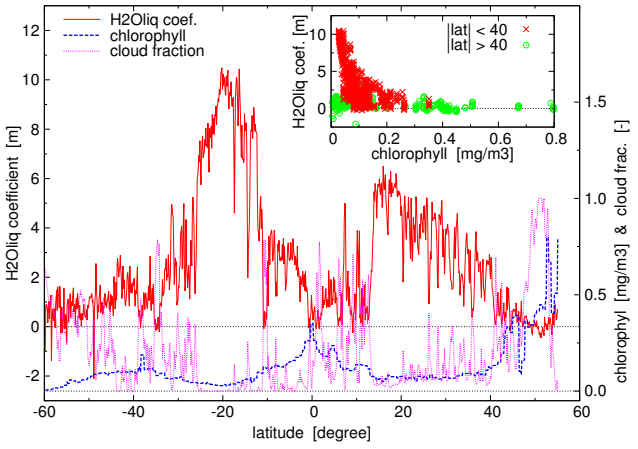

Figure 8. Retrieved H_2O_{liq} coefficient (in m; red solid line, left axis) as a function of latitude for row 29 of the Pacific Ocean test orbit, showing only ground pixels for which chlorophyll concentration data are available. Also shown, with values along the right axis, are the chlorophyll concentration (in mg m^{-3}; blue dashed line) and the cloud cover fraction (magenta dotted line). The inset shows the H_2O_{liq} coefficient as a function of the chlorophyll concentration separately for ground pixels with latitudes between $\pm 40°$ (red crosses) and higher latitudes (green circles).

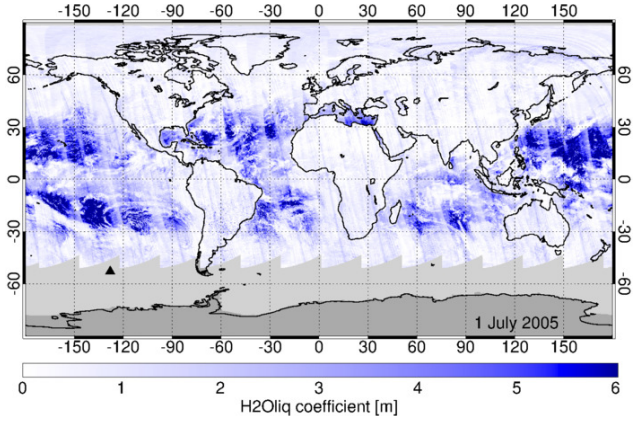

Figure 9. World map of the H_2O_{liq} coefficient (in m) based on all 15 OMI orbits of 1 July 2005; the Pacific Ocean test orbit is marked by a black triangle. All ground pixels with solar zenith angle less than 75° are plotted; no filtering for cloudy pixels was applied.

6 % and the retrieved H_2O_{liq} fit coefficients are physically meaningful: for pixel 425 the H_2O_{liq} fit coefficient is 10.49 m and for pixel 592 it is 0.83 m.

Figure 8 shows the retrieved H_2O_{liq} coefficient (left axis, red solid line) as a function of latitude for all ground pixels of detector row 29 for which a chlorophyll concentration is available. For comparison the graphs also shows the chlorophyll concentration and the cloud fraction for the same pixels (right axis); cloudiness clearly leads to lower H_2O_{liq} coefficients, as expected. The inset of Fig. 8 shows the relationship between the H_2O_{liq} coefficient and the chlorophyll concentration. The graph makes a distinction between the ground pixels in the latitude range 40° S to 40° N (red crosses) and outside that range (green circles). Pixels at latitudes above 40° N have chlorophyll concentration > 0.3 mg m^{-3} and for that reason low H_2O_{liq} coefficients. Pixels at latitudes $<$ 40° S at high solar zenith angle (above 70°) have low H_2O_{liq} coefficients (below about 2 m) even though chlorophyll concentrations are low (< 0.2 mg m^{-3}).

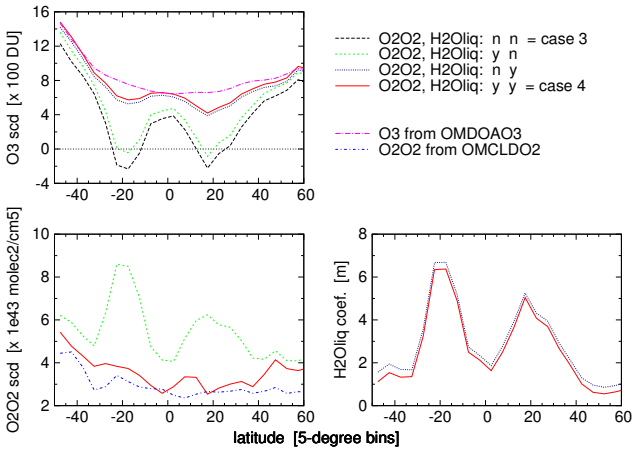

Figure 10. Retrieved values for the O_3 SCD (top-left), the O_2–O_2 SCD (bottom-left) and H_2O_{liq} coefficient (bottom-right) as a function of latitude for the Pacific Ocean test orbit for retrievals without and with absorption by O_2–O_2 and H_2O_{liq} included in the fit as specified by the legend in the top-right corner; case numbers 3 (black dashed) and 4 (red solid) refer to the cases listed in Table 4. Also plotted are the O_3 SCD value from the OMI ozone slant column product OMDOAO3 (magenta long-dash-dotted) and the O_2–O_2 SCD value from the OMCLDO2 cloud product (blue short-dash-dotted).

Figure 9 shows a global map of the H_2O_{liq} coefficient retrieved from all OMI orbits of 1 July 2005. Open water areas are clearly visible on the map and land/sea boundaries show up sharply in areas like the Mediterranean Sea, the Gulf of Mexico, around Madagascar and the east coast of South America. Along the west coasts of South America, North America and Africa, for example, the H_2O_{liq} coefficient is very low, consistent with high chlorophyll concentrations there. Note that since the processing is not optimised for the retrieval of the H_2O_{liq} coefficient, it is not possible to say how accurate the coefficient is, but overall its values appear realistic. Positive H_2O_{liq} fit coefficients over areas with little or no liquid water absorption, such as over land or cloudy scenes, are small.

The inclusion of the absorption of H_2O_{liq} and the O_2–O_2 collision complex in the NO_2 fit is justified since their absorption is known to affect the radiance $I(\lambda)$ – unless their inclusion would reduce the quality of the NO_2 fit, which is not the case. Figure 10 shows the effect of including O_2–O_2 and H_2O_{liq} in the retrieved O_3 SCDs. Without either of the two additional absorbers, ozone slant columns are negative

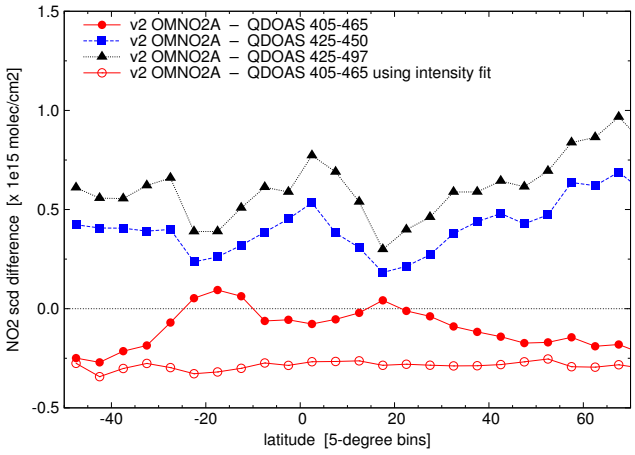

Figure 11. Differences of the NO_2 SCD values of the new v2 OMNO2A fit results (i.e. the red line with circles in Fig. 6) with QDOAS retrievals using different fit windows with a linear fitting approach (filled symbols) and using a non-linear fitting approach in the standard fit window (open circles) for the Pacific Ocean test orbit. The size of the steps along the vertical scale is the same as in Fig. 4 to ease comparison of the SCD differences.

in the regions where absorption in open water is taking place. Adding both absorbers brings the retrieved O_3 SCD close to the values given in the official OMI ozone SCD data product OMDOAO3; the improvement is mostly due to including H_2O_{liq} absorption.

Including O_2–O_2 absorption but not H_2O_{liq} absorption does not result in realistic O_3 SCD values. Furthermore, the retrieved O_2–O_2 SCD values appear realistic compared to the values given in the official OMI cloud data product OMCLDO2 if H_2O_{liq} is included in the fit. Including O_2–O_2 absorption has a small effect on the retrieved H_2O_{liq} coefficient (bottom-right panel in Fig. 10).

In summary, (a) including liquid water absorption leads to significant improvements in the NO_2 retrieval fit for pixels over clear open waters, without affecting other pixels, results in physically meaningful H_2O_{liq} and O_3 absorption coefficients; and (b) simultaneously including O_2–O_2 absorption results in realistic O_2–O_2 SCDs and improves the fit, especially if light paths are long.

5.3 Comparison between OMNO2A and QDOAS

Since the OMI, SCIAMACHY and GOME-2 spectral fits have been done with different fitting approaches and fitting windows (cf. Table 1), the sensitivity of the NO_2 SCD to the spectral fitting approach is studied here. Such estimates are important for satellite intercomparisons and the generation of long-term seamless multi-sensor data records such as the QA4ECV project. The flexible QDOAS package (version 2.105, May 2013), which provides a linear fit approach (cf. the details on DOAS fitting in Sect. S1 in the Supplement), is used for this study with the v2014 reference spectra on the OMI Pacific Ocean test orbit.

Figure 11 shows that the OMNO2A and QDOAS processors, both applied in the 405–465 nm window, result in small differences in the NO_2 SCDs of -0.2 to $+0.1 \times 10^{15}$ molec cm^{-2}. The agreement between these two is therefore quite good considering there are several differences between the processors: the fitting method differs, the Ring effect is included differently and the wavelength calibration of QDOAS differs from the OMNO2A wavelength calibration.

QDOAS has the option to apply a non-linear intensity fitting method instead of the linear optical density fitting method Eq. (S4), similar to the OMNO2A non-linear fitting method Eq. (1) but with the Ring effect treated as a pseudo-absorber; cf. Eq. (S5). The red line with open circles in Fig. 11 shows the difference between the results of this approach and the OMNO2A results, which appears to be larger than the difference with the linear fitting method of QDOAS: about -0.3×10^{15} molec cm^{-2}, almost independent of latitude.

The SCIAMACHY and GOME-2 NO_2 data are retrieved in the fit window 425–450 nm, using a third-degree polynomial. The difference between the OMI orbit processed with QDOAS in this manner and the OMNO2A data is shown by the blue line with squares in Fig. 11. At +0.2–0.6×10^{15} molec cm^{-2}, the difference is clearly larger than for the OMNO2A fit window.

In their study to improve the GOME-2 NO_2 retrieval, Richter et al. (2011) apply the extended fit window 425–497 nm. The black line with triangles in Fig. 11 shows that OMNO2A is higher by 0.4–0.9×10^{15} molec cm^{-2} than applying a linear fit in this extended fit window.

The NO_2 SCD differences in Fig. 11 show a clear latitudinal variation around latitudes 20° S and 20° N – areas of the Pacific Ocean where absorption in liquid water plays a role (cf. Sect. 5.2) – for the three curves where QDOAS was used in the linear fitting mode, while for QDOAS's non-linear fitting mode the differences with OMNO2A are nearly independent of latitude. This may indicate that the linear fitting method deals differently with the polynomial-like signature of H_2O_{liq} and/or O_3 and/or O_2–O_2 absorption (cf. Fig. S6) than the non-linear fitting method, which is possibly due to interference of the reference spectra with the DOAS polynomial (a few further remarks regarding this issue are given in Sect. S6).

In summary, the selection of the fit window (and with that the degree of the polynomial) and the fitting method determines the NO_2 fit results, i.e. there is no "true" NO_2 SCD but at most a fit window and fit method specific slant column value. Judging from the curves in Fig. 11, the variability in the fit window and fit method selection introduces differences in the retrieved NO_2 SCD between -0.3 and $+0.6 \times 10^{15}$ molec cm^{-2} (i.e. up to 0.2×10^{15} molec cm^{-2} in terms of the NO_2 VCD). To better understand the "true"

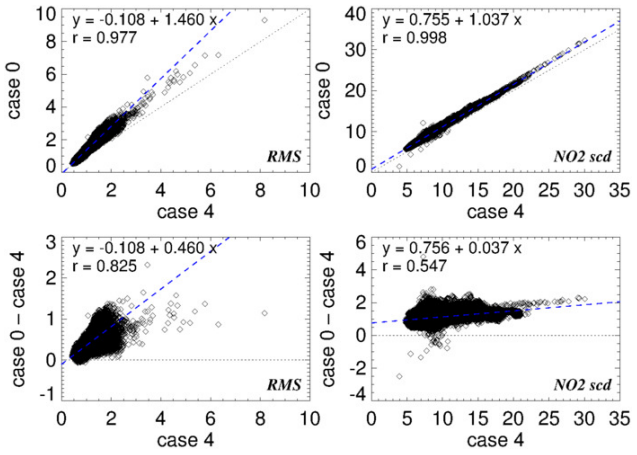

Figure 12. Scatter plots of current data (case 0, top row) and absolute differences between the current and the updated data (bottom row) of the RMS error (left column, $\times 10^{-4}$) and NO_2 SCD (right column, $\times 10^{15}$ molec cm^{-2}) as a function of the updated data (case 4) using the July 2005 average gridded data. Dashed blue lines show linear fits through the data; the fit and correlation coefficients are shown in the top-left of each graph.

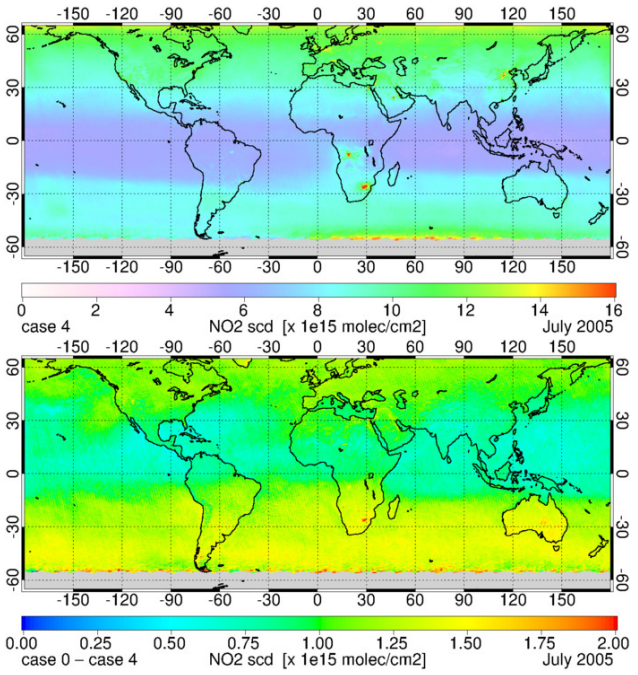

Figure 13. Monthly average gridded updated (case 4; top panel) NO_2 slant column data for July 2005 and the corresponding difference with the current (case 0) data (lower panel).

NO_2 SCD, a comparison with measurements that do not depend on the DOAS technique is needed.

5.4 Reprocessed OMI NO_2 data of 2005

All OMI NO_2 slant column data of the year 2005 have been reprocessed to evaluate the consistency of the proposed improvements. Figure 12 shows the current (case 0) data on the top row and the difference between the current and update data on the bottom row as a function of the updated (case 4) data. The linear relationship between the NO_2 SCD of the current and updated retrieval in the top-right panel shows an offset, reflecting the improved wavelength calibration. The slope of the linear fit is 1.04, which implies that high NO_2 SCD values will decrease more than low SCDs but not by much. This suggests that the effect of the updated retrieval settings on high (tropospheric) NO_2 SCDs will be small compared to the overall decrease of the NO_2 values.

Figure 13 shows a map of the monthly average gridded NO_2 slant columns of the updated (case 4) data and the corresponding difference with the current (case 0) data for July 2005. The RMS error data for the same month are shown in Fig. 14. Similar maps of the month of January 2005 are shown in Sect. S7 in the Supplement. In some areas with high NO_2 levels related to pollution, the decrease of the NO_2 slant column is relatively large, such as for the Highveld area in South Africa in Fig. 13 for July. The average change in the RMS error shown in the lower panel of Fig. 14 is about 0.33×10^{-4}. For clear-sky pixels only (not shown), the decrease of the RMS is much smaller, namely 0.14×10^{-4} on average, while for cloudy pixels (not shown) the decrease is much larger: 0.80×10^{-4} on average. Notably above clouds, the quality of the fit is evidently improved by the changes made to the OMNO2A retrieval.

Section S7 in the Supplement shows monthly average maps for July 2005 similar to Figs. 13–14 of the results of the other fit parameters.

6 Concluding remarks

The OMI NO_2 slant column density retrieval, OMNO2A, lies at the basis of the stratospheric and tropospheric NO_2 vertical column data products of OMI, notably the Dutch OMI NO_2 (DOMINO) and NASA SP data sets. This paper describes important updates for OMNO2A in order to improve the quality of the OMI NO_2 SCD data. The investigation was triggered by the high bias in OMI stratospheric NO_2 columns w.r.t. other satellite sensors and ground-based measurements as well as the need to investigate a number of other elements of the OMNO2A processor. The improvements for the OMNO2A processor are

- implementation of the wavelength and viewing angle dependency of the OMI slit function,
- optimisation of the wavelength calibration window based on minimising RMS and NO_2 errors,
- an update of the reference spectra of the trace gases included in the spectral fit,
- inclusion of absorption by O_2–O_2 and H_2O_{liq} to further reduce the RMS error.

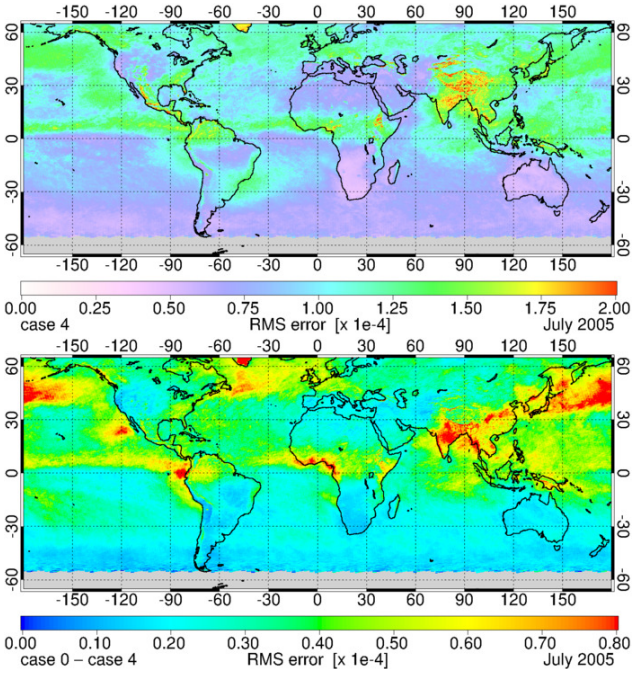

Figure 14. Monthly average gridded updated (case 4; top panel) RMS error data for July 2005 and the corresponding difference with the current (case 0) data (lower panel).

The updates of the wavelength calibration have the effect of removing an additive offset in the NO_2 SCD of 0.85×10^{15} molec cm^{-2} and reducing the RMS by about 23 % on average. The updates of trace gas reference spectra and the improved use of the OMI slit function for the convolution of these spectra lead to a reduction of the NO_2 SCD that depends on latitude, mainly related to the inclusion of O_2–O_2 absorption, varying from 0.2 to 0.6×10^{15} molec cm^{-2} (on average 0.35×10^{15} molec cm^{-2}); the RMS is reduced by about 9 % on average.

Absorption by the O_2–O_2 collision complex increases with solar zenith angle due to increased light path length and is therefore important at higher latitudes, and the resulting O_2–O_2 SCDs have realistic values. Accounting for absorption by liquid water (H_2O_{liq}) is particularly important for pixels over clear open waters with low chlorophyll concentrations and results in marked improvements of the spectral fit and assures that O_3 SCDs in the fit window have physically realistic values. Inclusion does not deteriorate the spectral fit for other, non-clear water pixels. The values found for the H_2O_{liq} fit coefficient are physically meaningful for the areas where absorption in liquid water is relevant.

NO_2 SCD retrievals for other satellite and ground-based instruments employ different spectral fit windows and use different implementations of the DOAS technique, which leads to small differences in the resulting SCD values. A short investigation of this using the QDOAS software (Danckaert et al., 2012) shows that the uncertainty in NO_2 SCD related to the choice of the fit window and fit method may be as large as 0.3×10^{15} molec cm^{-2}.

The combination of improvements to the OMNO2A spectral fit lead to an overall reduction of the NO_2 SCD by about 1.2×10^{15} molec cm^{-2}, a reduction of the NO_2 fitting error by 0.2–0.3 $\times 10^{15}$ molec cm^{-2} and a reduction of the RMS by 24–35 %. The reduction of the SCD is largely an additive offset, implying that the improvements in OMNO2A will probably affect stratospheric NO_2 most and smaller effects may be expected on tropospheric NO_2.

Comparing the updated OMNO2A data with SCIAMACHY data over the Pacific Ocean shows that the discrepancy between the two instruments is reduced from 1.2 to 0.8×10^{15} molec cm^{-2}. The remaining difference can be explained largely by the difference expected due to the diurnal cycle of stratospheric NO_2, which is higher by about 0.5×10^{15} molec cm^{-2} at 13:40 LT (when OMI measures) than at 09:30 (when SCIAMACHY measures), the different choice of the fitting window and the low bias of SCIAMACHY relative to other instruments.

The updates to the OMNO2A retrieval systems are sufficient to remove the bias between the stratospheric NO_2 columns from OMI and those from other satellite and ground-based instruments. A final test of this requires the conversion of the retrieved SCD to the separate stratospheric and tropospheric NO_2 columns. This issue will be discussed in a forthcoming study that describes improvements to the data assimilation system of DOMINO, leading to a new DOMINO v3.0 data set for the entire OMI period. The settings of the updated OMNO2A processing will be the initial configuration of the NO_2 retrieval for TROPOMI for reasons of consistency (van Geffen et al., 2014).

The Supplement related to this article is available online at doi:10.5194/amt-8-1685-2015-supplement.

Acknowledgements. This work is funded by the Netherlands Space Office (NSO). The authors would like to thank N. Krotkov, S. Marchenko, A. Richter and P. Valks for discussions and information on their approaches and studies. The authors would further like to thank Johan de Haan for discussions on and help with retrieval issues. Folkert Boersma acknowledges funding from NWO (Vidi grant 864.09.001) and support by the EU-FP7 grant QA4ECV (no. 607405). The research at BIRA-IASB (AGACC-II project) and the University of Liège (A3C and ACROSAT projects from the PRODEX program) has been financially supported by the Belgian Federal Science Policy Office (BELSPO), Brussels, and via the EU 7th Framework Programme project NORS (contract 284421). BIRA-IASB is thankful to M. P. Chipperfield (University of Leeds) for providing SLIMCAT data. The authors would also like to thank the International Foundation High Altitude Research Stations Jungfraujoch and Gornergrat (HFSJG, Bern).

Edited by: J. Stutz

References

Beirle, S., Boersma, K. F., Platt, U., Lawrence, M. G., and Wagner T.: Megacity emissions and lifetimes of nitrogen oxides probed from space, Science, 333, 1737–1739, doi:10.1126/science.1207824, 2011.

Beirle, S., Sihler, H., and Wagner, T.: Linearisation of the effects of spectral shift and stretch in DOAS analysis, Atmos. Meas. Tech., 6, 661–675, doi:10.5194/amt-6-661-2013, 2013.

Belmonte-Rivas, M., Veefkind, P., Boersma, F., Levelt, P., Eskes, H., and Gille, J.: Intercomparison of daytime stratospheric NO_2 satellite retrievals and model simulations, Atmos. Meas. Tech., 7, 2203–2225, doi:10.5194/amt-7-2203-2014, 2014.

Boersma, K. F., Eskes, H. J., and Brinksma, E.J.: Error analysis for tropospheric NO_2 retrieval from space, J. Geophys. Res., 109, D04311, doi:10.1029/2003JD003962, 2004.

Boersma, K. F., Eskes, H. J., Veefkind, J. P., Brinksma, E. J., van der A, R. J., Sneep, M., van den Oord, G. H. J., Levelt, P. F., Stammes, P., Gleason, J. F., and Bucsela, E. J.: Near-real time retrieval of tropospheric NO_2 from OMI, Atmos. Chem. Phys., 7, 2103–2118, doi:10.5194/acp-7-2103-2007, 2007.

Boersma, K. F., Eskes, H. J., Dirksen, R. J., van der A, R. J., Veefkind, J. P., Stammes, P., Huijnen, V., Kleipool, Q. L., Sneep, M., Claas, J., Leitão, J., Richter, A., Zhou, Y., and Brunner, D.: An improved tropospheric NO_2 column retrieval algorithm for the Ozone Monitoring Instrument, Atmos. Meas. Tech., 4, 1905–1928, doi:10.5194/amt-4-1905-2011, 2011.

Bogumil, K., Orphal, J., and Burrows, J. P.: Temperature dependent absorption cross sections of O_3, NO_2, and other atmospheric trace gases measured with the SCIAMACHY spectrometer, in Looking down to Earth in the New Millennium, Proceedings of the ERS-ENVISAT Symposium, 16–20 October 2000, Gothenburg, Sweden, ESA publication SP-461, 2000.

Bovensmann, H., Burrows, J. P., Buchwitz, M., Frerick, J., Noel, S., Rozanov, V. V., Chance, K. V., and Goede, A. P. H.: SCIAMACHY: Mission objectives and measurement modes, J. Atmos. Sci., 56, 127–150, 1999.

Bucsela, E. J., Celarier, E. A., Wenig, M. O., Gleason, J. F., Veefkind, J. P., Boersma, K. F., and Brinksma, E. J.: Algorithm for NO_2 vertical column retrieval from the ozone monitoring instrument, IEEE Trans. Geosci. Rem. Sens., 44, 1245–1258, doi:10.1109/TGRS.2005.863715, 2006.

Bucsela, E. J., Krotkov, N. A., Celarier, E. A., Lamsal, L. N., Swartz, W. H., Bhartia, P. K., Boersma, K. F., Veefkind, J. P., Gleason, J. F., and Pickering, K. E.: A new stratospheric and tropospheric NO_2 retrieval algorithm for nadir-viewing satellite instruments: applications to OMI, Atmos. Meas. Tech., 6, 2607–2626, doi:10.5194/amt-6-2607-2013, 2013.

Burrows, J. P., Weber, M., Buchwitz, M., Rozanov, V., Ladstätter-Weißenmayer, A., Richter, A., Debeek, R., Hoogen, R., Bramstedt, K., Eichmann, K.-U., Eisinger, M., and Perner, D.: The Global Ozone Monitoring Experiment (GOME): Mission concept and first results, J. Atmos. Sci., 56, 151–175, 1999.

Chance, K. V. and Spurr, R. J. D.: Ring effect studies: Rayleigh scattering, including molecular parameters for rotational Raman scattering, and the Fraunhofer spectrum, Appl. Optics, 36, 5224–5230, 1997.

Crutzen, P. J.: The influence of nitrogen oxides on the atmospheric ozone content, Q. J. Roy. Meteor. Soc., 96, 320–325, 1970.

Danckaert, T., Fayt, C., and Van Roozendael, M. QDOAS software user manual, Version 2.1, December 2012, BIRA-IASB, Brussels, Belgiun, 2012.

Dirksen, R., Dobber, M. R., Voors, R., and Levelt, P.: Pre-launch characterization of the Ozone Monitoring Instrument transfer function in the spectral domain, Appl. Optics, 45, 3972–3981, doi:10.1364/AO.45.003972, 2006.

Dirksen, R. J., Boersma, K. F., Eskes, H. J., Ionov, D. V., Bucsela, E. J., Levelt, P. F., and Kelder, H. M.: Evaluation of stratospheric NO_2 retrieved from the Ozone Monitoring Instrument: Intercomparison, diurnal cycle, and trending, J. Geophys. Res. 116, D08305, doi:10.1029/2010JD014943, 2011.

Dobber, M., Voors, R., Dirksen, R., Kleipool, Q., and Levelt, P.: The high-resolution solar reference spectrum between 250 and 550 nm and its application to measurements with the Ozone Monitoring Instrument, Sol. Phys., 249, 281–291, doi:10.1007/s11207-008-9187-7, 2008.

Fuglestvedt, J. S., Berntsen, T., Isaksen, I. S. A., Mao, H., Liang, X.-Z., and Wang, W.-C.: Climatic forcing of nitrogen oxides through changes in tropospheric ozone and methane, Atmos. Environ., 33, 961–977, doi:10.1016/s1352-2310(98)00217-9, 1999.

Grainger, J. F. and Ring, J.: Anomalous Fraunhofer line profiles, Nature, 193, p. 762, doi:10.1038/193762a0, 1962.

Hendrick, F., Mahieu, E., Bodeker, G. E., Boersma, K. F., Chipperfield, M. P., De Maziére, M., De Smedt, I., Demoulin, P., Fayt, C., Hermans, C., Kreher, K., Lejeune, B., Pinardi, G., Servais, C., Stübi, R., van der A, R., Vernier, J.-P., and Van Roozendael, M.: Analysis of stratospheric NO_2 trends above Jungfraujoch using ground-based UV-visible, FTIR, and satellite nadir observations, Atmos. Chem. Phys., 12, 8851–8864, doi:10.5194/acp-12-8851-2012, 2012.

Krotkov, N. A., Bucsela, E. J., Celarier, E. A., Lamsal, L. N., and Swartz, W. H.: Improved OMI NO2 Standard Product: Algorithm, evaluation, and results, EOS Aura Science Team Meeting, Pasadena, CA, USA, 1–3 October, 2012.

Lerot, C., Van Roozendael, M., van Geffen, J., van Gent, J., Fayt, C., Spurr, R., Lichtenberg, G., and von Bargen, A.: Six years of total ozone column measurements from SCIAMACHY nadir observations, Atmos. Meas. Tech., 2, 87–98, doi:10.5194/amt-2-87-2009, 2009.

Lerot, C., Stavrakou, T., De Smedt, I., Müller, J.-F., and Van Roozendael, M.: Glyoxal vertical columns from GOME-2 backscattered light measurements and comparisons with a global model, Atmos. Chem. Phys., 10, 12059–12072, doi:10.5194/acp-10-12059-2010, 2010.

Leue, C.: Detektion der troposphärischen NO_2 Daten anhand von GOME, PhD thesis, Univ. Heidelberg, Heidelberg, Germany, 1999.

Levelt, P. F., van den Oord, G. H. J., Dobber, M. R., Mälkki, A., Visser, H., de Vries, J., Stammes, P., Lundell, J. O. V., and Saari, H.: The Ozone Monitoring Instrument, IEEE Trans. Geosci. Rem. Sens., 44, 1093–1101, doi:10.1109/tgrs.2006.872333, 2006.

Munro, R., Eisinger, M., Anderson, C., Callies, J., Corpaccioli, E. Lang, R., Lefebvre, A., Livschitz, Y., and Albinana, A. P.: GOME-2 on MetOp, ESA publication SP 628, Paris, France, 2006.

Murphy, D. M., Fahey, D. W., Proffitt, M. H., Liu, S. C., Chan, K. R., Eubank, C. S., Kawa, S. R., and Kelly, K. K.: Reactive

nitrogen and its correlation with ozone in the lower stratosphere and upper troposphere, J. Geophys. Res., 98, 8751–8773, 1993.

Peters, E., Wittrock, F., Richter, A., Alvarado, L. M. A., Rozanov, V. V., and Burrows, J. P.: Liquid water absorption and scattering effects in DOAS retrievals over oceans, Atmos. Meas. Tech., 7, 4203–4221, doi:10.5194/amt-7-4203-2014, 2014.

Platt, U.: Differential Optical Absorption Spectroscopy (DOAS), in: Air monitoring by spectroscopic techniques, edited by: M. W. Sigrist, Chemical Analisys Series, 127, 27–76, Wiley, New York, USA, 1994.

Platt, U. and Stutz, Z.: Differential Optical Absorption Spectroscopy, Principles and Applications, Springer, Heidelberg, Germany, 597 pp., 2008.

Pope, R. M. and Fry, E. S.: Absorption spectrum (380–700 mnm) of pure water. II. Integrating cavity measurements, Appl. Optics, 36, 8710–8723, doi:10.1364/AO.36.008710, 1997.

Richter, A., Begoin, M., Hilboll, A., and Burrows, J. P.: An improved NO_2 retrieval for the GOME-2 satellite instrument, Atmos. Meas. Tech., 4, 1147–1159, doi:10.5194/amt-4-1147-2011, 2011.

Rothman, L. S., Gordon, I. E., Babikov, Y., Barbe, A., Chris Benner, D., Bernath, P. F., Birk, M., Bizzocchi, L., Boudon, V., Brown, L. R., Campargue, A., Chance, K., Cohen, E. A., Coudert, L. H., Devi, V. M., Drouin, B. J., Fayt, A., Flaud, J.-M., Gamache, R. R., Harrison, J. J., Hartmann, J.-M., Hill C., Hodges, J. T., Jacquemart, D., Jolly, A., Lamouroux, J., Le Roy, R. J.,Li, G., Long, D. A., Lyulin, O. M., Mackie, C. J., Massie, S. T., Mikhailenko, S., Müller, H. S. P., Naumenko, O. V., Nikitin, A. V., Orphal, J., Perevalov, V., Perrin, A., Polovtseva, E. R., Richard, C., Smith, M. A. H., Starikova, E., Sung, K., Tashkun, S., Tennyson, J., Toon, G. C., Tyuterev, Vl. G., and Wagn, G.: The HITRAN 2012 molecular spectroscopic database, J. Quant. Spectrosc. Ra., 130, 4–50, doi:10.1016/j.jqsrt.2013.07.002, 2013.

Schaub, D., Brunner, D., Boersma, K. F., Keller, J., Folini, D., Buchmann, B., Berresheim, H., and Staehelin, J.: SCIAMACHY tropospheric NO_2 over Switzerland: estimates of NO_x lifetimes and impact of the complex Alpine topography on the retrieval, Atmos. Chem. Phys., 7, 5971–5987, doi:10.5194/acp-7-5971-2007, 2007.

Shindell, D. T., Faluvegi, G., Koch, D. M., Schmidt, G. A., Unger, N., and Bauer, S. E.: Improved attribution of climate forcing to emissions, Science, 326, 716–718, doi:10.1126/science.1174760, 2009.

Sillman, S., Logan, J. A., and Wofsy, S. C.: The sensitivity of ozone to nitrogen oxides and hydrocarbons in regional ozone episodes, J. Geophys. Res., 95, 1837–1851, 1990.

Stutz, J. and Platt, U.: Numerical analysis and estimation of the statistical error of differential optical absorption spectroscopy measurements with least-squares methods, Appl. Opt., 35, 6041–6053, doi:10.1364/AO.35.006041, 1996.

Thalman, R. and Volkamer, R.: Temperature dependant absorption cross-sections of O_2-O_2 collision pairs between 340 and 630 nm at atmospherically relevant pressure, Phys. Chem. Chem. Phys., 15, 15371–15381, doi:10.1039/C3CP50968K, 2013.

van Geffen, J. H. G. M., Boersma K. F., Eskes, H. J., Maasakkers, J. D., and Veefkind, J.P.: TROPOMI ATBD of the total and tropospheric NO_2 data products, Report S5P-KNMI-L2-0005-RP version 0.11.0, 2 October 2014, KNMI, De Bilt, the Netherlands, 2014.

Van Roozendael, M., Loyola, D., Spurr, R., Balis, D., Lambert, J.-C., Livschitz, Y., Valks, P., Ruppert, T., Kenter, P., Fayt, C., and Zehner, C.: Ten years of GOME/ERS-2 total ozone data – The new GOME data processor (GDP) version 4: 1. Algorithm description, J. Geophys. Res., 111, D14311, doi:10.1029/2005JD006375, 21 pp., 2006.

Vandaele A. C., Hermans, C., Simon, P. C., Carleer, M., Colin, R., Fally, S., Mérienne, M. F., Jenouvrier, A., and Coquart, B.: Measurements of the NO_2 absorption cross-section from 42 000 cm^{-1} to 10 000 cm^{-1} (238–1000 nm) at 220 K and 294 K, J. Quant. Spectrosc. Ra., 59, 171–184, 1998.

Vasilkov, A. P., Joiner, J., Gleason, J., and Bhartia, P. K.: Ocean Raman scattering in satellite backscatter UV measurements, Geophys. Res. Lett., 29, 1837–1840, doi:10.1029/2002GL014955, 2002.

Veefkind, J. P., Aben, I., McMullan, K., Förster, H., de Vries, J., Otter, G., Claas, J., Eskes, H. J., de Haan, J. F., Kleipool, Q., van Weele, M., Hasekamp, O., Hoogeveen, R., Landgraf, J., Snel, R., Tol, P., Ingmann, P., Voors, R., Kruizinga, B., Vink, R., Visser, H., and Levelt, P. F.: TROPOMI on the ESA Sentinel-5 Precursor: A GMES mission for global observations of the atmospheric composition for climate, air quality and ozone layer applications, Remote Sens. Environ., 120, 70–83, doi:10.1016/j.rse.2011.09.027, 2012.

Voors, R., Dirksen, R., Dobber, M., and Levelt, P.: OMI in-flight wavelength calibration and the solar reference spectrum, in: Proceedings of the First Converence on Atmospheric Science, 8–12 May 2006, ESA publication SP-628, Frascati, Italy, 6 pp., 2006.

Vountas, M., Richter, A., Wittrock, F., and Burrows, J. P.: Inelastic scattering in ocean water and its impact on trace gas retrievals from satellite data, Atmos. Chem. Phys., 3, 1365–1375, doi:10.5194/acp-3-1365-2003, 2003.

World Health Organisation: Health Aspects of Air Pollution with Particulate Matter, Ozone and Nitrogen Dioxide, World Health Organisation, Bonn, Germany, 98 pp., 2003.